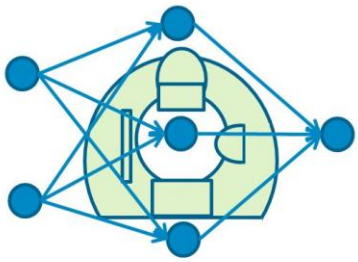

IMPACT

Intelligence based iMprovement of Personalized medicine And Clinical workflow supporT

DELIVERABLE D3.1.1

State of the art on current MR based approaches for detecting and segmenting brain tumours

Project number:	ITEA 17021
Document version no.:	v 1.0
Edited by:	Anders Eklund, Linköping University
Date:	June 26, 2019

ITEA Roadmap domains:
Major: Group

ITEA Roadmap categories:
Major: Content & knowledge
Minor: Interaction

HISTORY

Document version #	Date	Remarks
V0.1	2019-05-15	First version, created by LiU, Elekta, SyntheticMR
V0.2	2019-05-28	Minor revisions
V0.3	2019-06-19	Revisions after review
V1.0	2019-06-26	Approved

Deliverable review procedure:

- **2 weeks before due date**: deliverable owner sends deliverable –approved by WP leader– to Project Manager
- **Upfront** PM assigns a co-reviewer from the PMT group to cross check the deliverable
- **1 week before due date**: co-reviewer provides input to deliverable owner
- **Due date:** deliverable owner sends the final version of the deliverable to PM and co-reviewer

TABLE OF CONTENTS

1 Glossary

ADC	Apparent diffusion coefficient
CNN	Convolutional neural network
DDE	Double diffusion encoding
DKI	Diffusion kurtosis imaging
DTI	Diffusion tensor imaging
ET	Enhanced tumour
GBM	Glioblastoma multiforme
MD	Mean diffusivity
MRI	Magnetic resonance imaging
QTI	Q-space trajectory imaging
SRS	Stereotactic radiosurgery
TC	Tumour core
WBRT	Whole brain radiotherapy
WT	Whole tumour

2 Introduction

Brain tumours affect the quality of life for a large number of persons, and it is therefore important that they can be detected in an early stage and treated. Brain tumours can become very large, and it is therefore beneficial to detect small tumours (e.g. metastases) before they grow into large tumours. Magnetic resonance imaging (MRI) enables non-invasive imaging without any ionizing radiation. Structural MRI (e.g. T1- (with and without gadolinium contrast) and T2-weighted anatomical images) is used for detecting and segmenting brain tumours, but other MRI sub-modalities, such as diffusion MRI and quantitative MRI, can add more information about the tumour type and where the border of the tumour is located.

In this report we will discuss the state of the art for MR based approaches for detecting and segmenting brain tumours and metastases. We will start with an overview of how common different brain tumour types are and how they can be treated. We will then cover how deep learning is currently being used for automatic segmentation. We will end by discussing recent research in diffusion MRI and quantitative MRI.

3 Overview of brain tumour types, how common they are and how they can be treated

A brain tumour is an abnormal growth of cells in the brain that is either benign or malignant (cancerous). Primary tumours grow from the brain tissue itself whereas secondary (metastatic) tumours have spread from cancer located in other parts of the body, sharing the cell type with the primary tumour. The cancer is classified either in different stages or in different grades. The stages are based on the spread in the body and differ depending on the body site of the cancer. The first stage corresponds to a small localized tumour and the fourth and last stage corresponds to a cancer that has metastasized to other sites in the body. Grading, on the other hand, depends on the microscopic properties of the cancerous cells and how much they differ from the healthy cells, where a low-graded tumour is clearly differentiated from healthy cells and a high-graded tumour is undifferentiated.

Depending on diagnosis, size and location of the tumour both treatment options and aim of the treatment vary. If possible, the first treatment step for primary tumours is surgical resection of the entire or parts of the tumour. This is often followed by stereotactic radiosurgery (SRS), fractionated radiotherapy or particle therapy to treat the remainder of the tumour or suspected tumour infiltration into the surrounding healthy tissue. Radiotherapy can be delivered despite the blood-brain barrier, which poses a problem for systemic treatments, such as chemotherapy, of brain tumours (Di Lorenzo et al., 2017).

The most common type of brain tumours are metastases, which occur in 20-40% of all cancer patients and most commonly metastasize from primary malignant lung cancer, breast cancer or melanoma. The efficiency of surgical resection of more than a single metastasis is debatable and since more than one metastasis is common at the time of diagnosis, whole brain radiotherapy (WBRT) has historically often been the treatment of choice. However, the use of WBRT is connected to severe side effects, primarily cognitive and neurological deficits after treatment (Brown et al., 2017). At the same time, the metastases are typically well circumscribed compared to primary brain tumours, and therefore they should present a suitable target for stereotactic radiosurgery (SRS), either as the only treatment or with adjuvant WBRT (Brown et al., 2018). For patients with less than five brain metastases, using SRS as the only treatment has proven equally effective as combined with WBRT, with the benefit of less side effects. For patients with a larger number of metastases, the use of only SRS treatment remains a matter of study (Sahgal et al., 2017). The response to radiotherapy of the brain tumours depends on the primary tumour and in recent time, targeted therapies have become increasingly more effective and therapeutic agents that can cross the blood-brain barrier have been identified. Therefore, treatment of brain metastases

has developed to include multimodal treatments and systemic therapies. Therefore, treatment can be combinations of surgery, radiotherapy, radiosurgery, chemotherapy, immunotherapy and targeted therapies.

Gliomas are malignant tumours that constitute about 30% of all tumours in the brain and central nervous system (Ostrom et al., 2018) and they are therefore the most common type of malignant primary brain tumour (Goodenberger and Jenkins, 2012). The gliomas arise in the glial cells, i.e. non-neuronal cells, in the central nervous system and there are several types of gliomas, among them glioblastoma multiforme (GBM), which is both the most aggressive and common primary malignant brain tumour among adults. GBM is almost always recurrent and the prognosis is poor, with less than 5% surviving more than 5 years (Davis, 2016). The treatment approach is aggressive, following the Stupp protocol, with maximally safe surgical resection of the tumour followed by the alkylating chemotherapy agent temozolomide (TMZ), normally complemented with radiotherapy. Given the size and invasive nature of the GBM, there are several limitations and risk factors including radiation necrosis and permanent neuronal damage induced by radiation (Curado et al., 2007; Iacob and Dinca, 2009). Despite the aggressive treatment the median survival after treatment is 15 months (Koshy et al., 2012). Therefore, large efforts are devoted to developing new treatments such as nanoparticles and refining targeted therapies, vaccines and immunotherapy strategies (Paolillo et al., 2018). The largest open dataset of brain tumours, i.e. the BraTS dataset (Menze et al., 2015), Figure 1, consists of GBM and lower grade gliomas and therefore these brain tumour types are the most studied in the context of deep learning and especially in image segmentation.

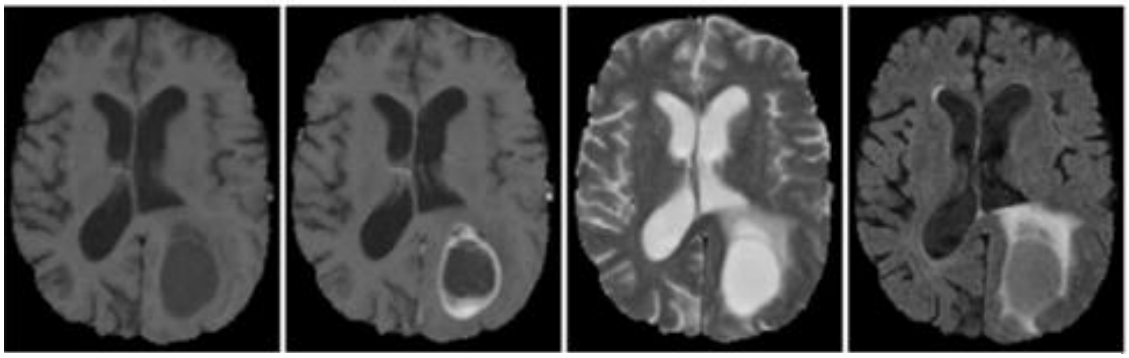

Figure 1. MR images of glioblastoma multiforme taken from the BraTS dataset (Menze et al., 2015). Images taken with (from left): T1, T1 after Gadolinium (Gd) contrast, T2 and T2 FLAIR.

Meningiomas are benign dural-based tumours that arise in the meninges and they are the most common intracranial tumour, although strictly speaking not a brain tumour, accounting for 35% of the primary brain tumours (Ostrom et al., 2018). They are typically grade I and slow growing with symptoms slowly increasing and can therefore become large before they are diagnosed. In most

cases, surgical resection of the meningioma or SRS alone is sufficient but at times it is necessary to complement the treatment with fractionated radiotherapy (Apra et al., 2018). For the rarer, recurrent and more aggressive type of meningioma, systemic treatments might be necessary when further surgery or radiotherapy is not possible (Le Rhun et al., 2016).

The second most common benign tumours are pituitary adenomas, accounting for approximately 15% of all brain primary tumours (Ostrom et al., 2018). They are slow-growing tumours arising from cells in pituitary gland. Functional pituitary adenomas produce an excess of hormones. The most common type is prolactinoma, i.e. tumours that cause increased prolactin levels causing e.g. amenorrhea in women and galactorrhea. More uncommon functional pituitary adenomas can be growth hormone secreting causing enlargement of e.g. lips, tongue and nose. Non-functioning adenomas present with symptoms caused by pressure of the tumour on nearby organs (Melmed 2011). For functional adenomas, treatment with hormone suppressing medicine, such as bromocripitine or cabergoline, is sufficient. These medicines block the excess hormones and the tumour often shrinks, but are often necessary to continue taking for the rest of the patient's life. If necessary, the treatment is supplemented with surgery and radiation. For non-functional adenomas, the treatment is similar to that of meningiomas. The first line of treatment is surgery, complemented with SRS and fractionated radiotherapy if necessary (Molitsch, 2016).

Vestibular Schwannomas, also known as acoustic neurinomas, arise in the Schwann cells of the eight cranial nerve. They are slowly growing benign tumours in the internal auditory canal that causes displacement of other organs, which might cause symptoms. In principle, it is not necessary to actively treat an asymptomatic non-growing vestibular schwannoma. Treatment of a vestibular schwannoma always comes at the risk of loss of hearing and damage to the facial nerve. An asymptomatic patient could therefore be held under regular observations during months or years without any intervention. If active treatment is necessary and the tumour is small to medium sized, SRS is the best option with high progression-free survival rate and long-term local tumour control. If the tumour is too large for SRS or the tumour presses on the brain stem, surgery is the best option (Tsao et al., 2017).

4 Overview of deep learning methods for tumour segmentation

Research about automatic segmentation of brain tumours is currently very focused on deep learning, where a convolutional neural network (CNN) is trained by showing MR images and corresponding ground truth (manual) tumour segmentations provided by an expert (e.g. a neuroradiologist). The segmentation can be performed using a single MR modality (e.g. a T1-weighted image) or by simultaneously showing several types of MR images to a multi-channel CNN (e.g. T1W, T1W with contrast, T2W, FLAIR). The annual BraTS (brain tumour segmentation) challenge (Menze et al., 2015) provides MR data for training and testing, and is one reason why deep learning has become so popular for brain tumour segmentation. We will here review the most successful (deep learning) contributions to BraTS 2017 and 2018, see Table 1. The interested reader is referred to D2.3.1 “State of the art on 3D segmentation using deep learning” for further information on deep learning segmentation.

Table 1. Overview of most successful segmentation approaches from BraTS 2018 and BraTS 2017. The contributions were ranked using a combination of Dice score and Hausdorff distance.

Publication	Overview
Myronenko (2018)	1st place in BraTS 2018. 3D encoder-decoder with additional VAE branch for encoder regularization.
Isensee et al. (2018)	2nd place in BraTS 2018. 3D U-Net with minor modifications.
McKinley et al. (2018)	3rd place (shared) in BraTS 2018. DenseNet structure with dilated convolutions embedded in U-Net-like network.
Zhou et al. (2018)	3rd place (shared) in BraTS 2018. Ensemble of different networks, with multi-scale context, cascade segmentations with shared backbone weights, and attention block.
Kamnitsas et al. (2017)	1st place in BraTS 2017. Ensemble of DeepMedic, FCN and 3d U-Net.
Wang et al. (2017)	2nd place in BraTS 2017.

The best results on the BraTS 2018 challenge were achieved by Myronenko (2018), see Figures 2 and 3 and Table 2. This work employs a 3D encoder-decoder architecture based on multiple ResNet-like blocks. As a novelty, the network is split into two decoding branches at the encoder endpoint output, where one of the branches is a regular decoder that produces the three tumour segmentation maps, and the other a variational decoder that reconstructs the input volume. This variational decoder branch serves as regularization for the shared encoder, and is only active during training.

Their model was trained on an NVidia Tesla V100 GPU with 32 GB of RAM, with large input crops of size 160x192x128, and using a batch size of 1, concatenating all 4 MRI modalities as input, and producing 3 nested tumour segmentations as output. A variety of augmentation strategies were used, including averaging the output of multiple flipped input images and ensembling multiple models trained from scratch.

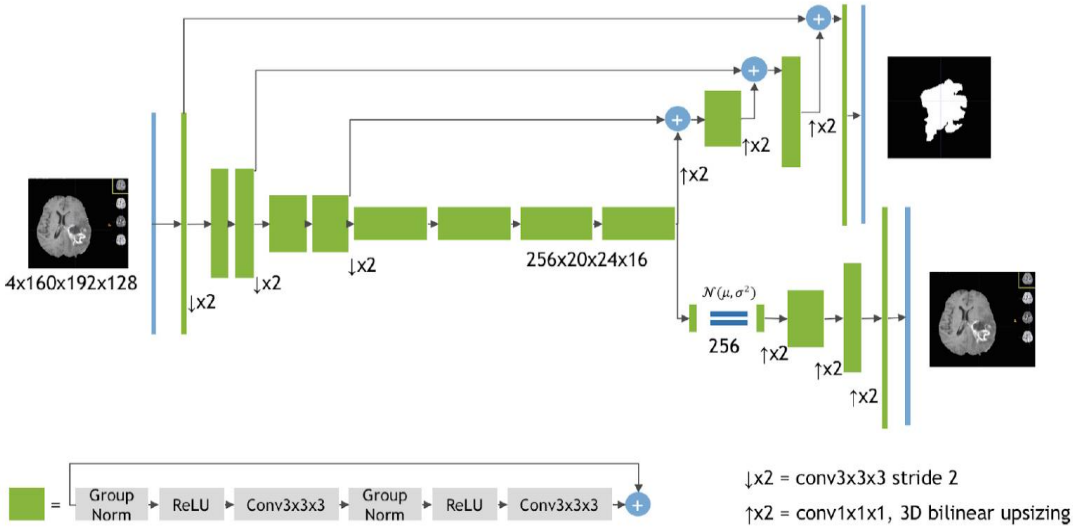

Figure 2. The encoder-decoder architecture employed in Myronenko (2018). The top decoder branch produces the tumour segmentation maps, while the bottom one reconstructs the input volume.

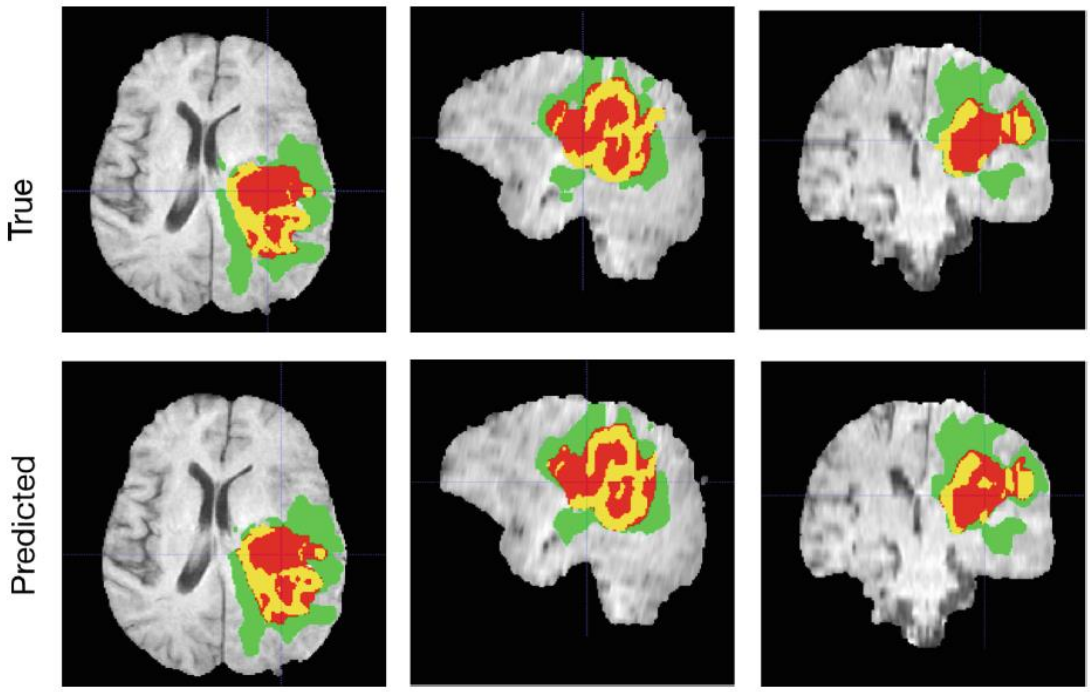

Figure 3. The segmentation results achieved in Myronenko (2018) are highly consistent with the ground truth. The whole tumor class includes all visible labels (a union of green, yellow and red labels), the tumor core class is a union of red and yellow, and the enhancing tumor core class is shown in yellow (a hyperactive tumor part).

Testing dataset	Dice			Hausdorff (mm)		
	ET	WT	TC	ET	WT	TC
Ensemble of 10 models	0.7664	0.8839	0.8154	3.7731	5.9044	4.8091

Table 2. Testing results from Myronenko (2018), which achieved the 1st place in the BraTS 2018 challenge. ET stands for enhanced tumour, WT stands for whole tumour, and TC stands for tumour core.

The second place in the challenge was taken by Isensee et al. (2018), who set out to and succeed in showing the potential of a well trained U-Net against the large number of modified encoder-decoder architectures used nowadays for segmentation. To that end they employed a 3D U-Net with only minor modifications, such as using Leaky ReLU activations and a multiclass Dice loss, see Figure 4.

Several measures were taken in order to counteract the limited graphics RAM provided by their 12 GB NVidia Titan X GPU, such as limiting the amount of filters before upsampling and using inplace operations whenever possible. These allowed a relatively large input patches of size 128x128x128 and four channels, while training with a batch size of 2. Additional performance was extracted from the incorporation of region based prediction (inspired by Wang et al. (2017)), co-training with additional datasets, postprocessing steps, and a joint Dice and cross-entropy loss function, see Figure 5 for some results.

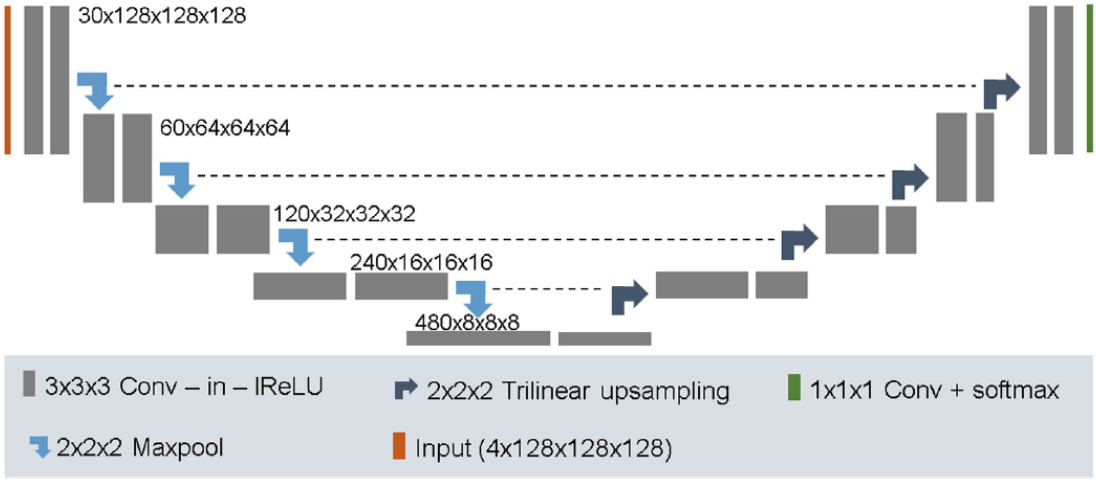

Figure 4. Straightforward 3D U-Net architecture employed in Isensee et al. (2018).

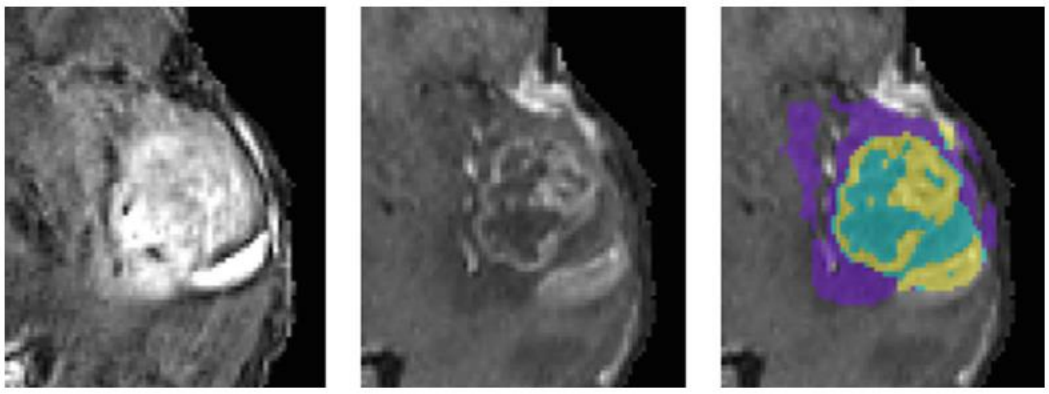

Figure 5. From left to right: FLAIR, T1 contrast agent enhanced, and example segmentation results from Isensee et al. (2018).

		Dice			Hausd. dist.		
		enh.	whole	core	enh.	whole	core
NVDLMED	Mean	76.64	88.39	81.54	3.77	5.90	4.81
	StdDev	25.57	11.83	24.99	8.61	10.01	7.52
	Median	84.41	92.06	91.67	1.73	3.16	2.45
MIC-DKFZ	Mean	77.88	87.81	80.62	2.90	6.03	5.08
	StdDev	23.93	12.89	25.02	3.85	9.98	8.09
	Median	84.94	91.79	90.72	1.73	3.16	2.83

Table 3. Comparison of winning BraTS 2018 entry (NVDLMED, Myronenko (2018)) and second place entry (MIC-DKFZ, Isensee et al. (2018)). Isensee et al. achieved better results for enhancing tumour, while Myronenko outperformed them in tumour core and whole tumour.

The third place in the challenge was shared between McKinley et al. (2018) and Zhou et al. (2018). McKinley et al. (2018) used a U-Net-like architecture with a series of DenseNet blocks between the encoding and decoding stages, and using dilated convolutions in place of pooling layers to increase the receptive field, see Figure 6. They also account for prediction uncertainty by having their network output both label predictions and the probability of a wrong prediction for each voxel, and use both of these quantities in their loss function.

Interestingly, the model employed takes as input 5 contiguous slices from each of the four available MRI modalities, and initial convolutions are performed in 3D, but after two convolution stages the slice blocks become two-dimensional, and 2D operations are applied in the remainder of the network. Predictions are made on a slice-by slice basis, and the model is trained and applied on slices in all three directions simultaneously. The final predictions are obtained by combining the outputs produced by two slightly different network architectures and predictions made with slices oriented in all three possible directions. See Figure 7 and Table 4 for some results.

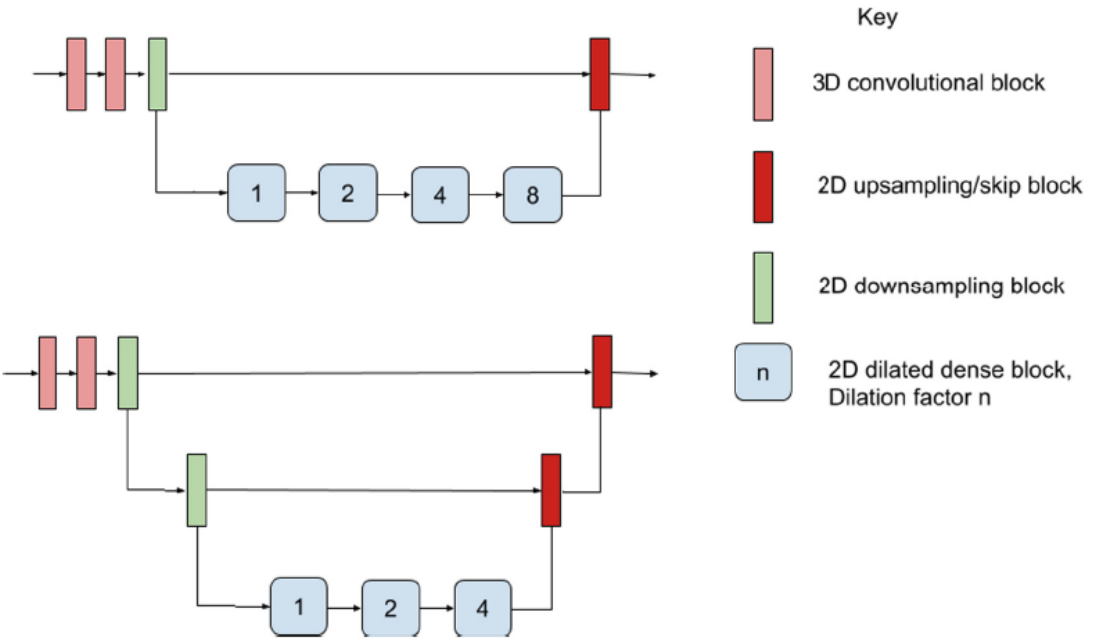

Figure 6. Two different network architectures employed in McKinley et al. (2018). The first two layers perform 3D convolutions, while the remainder of the networks works operates in 2D.

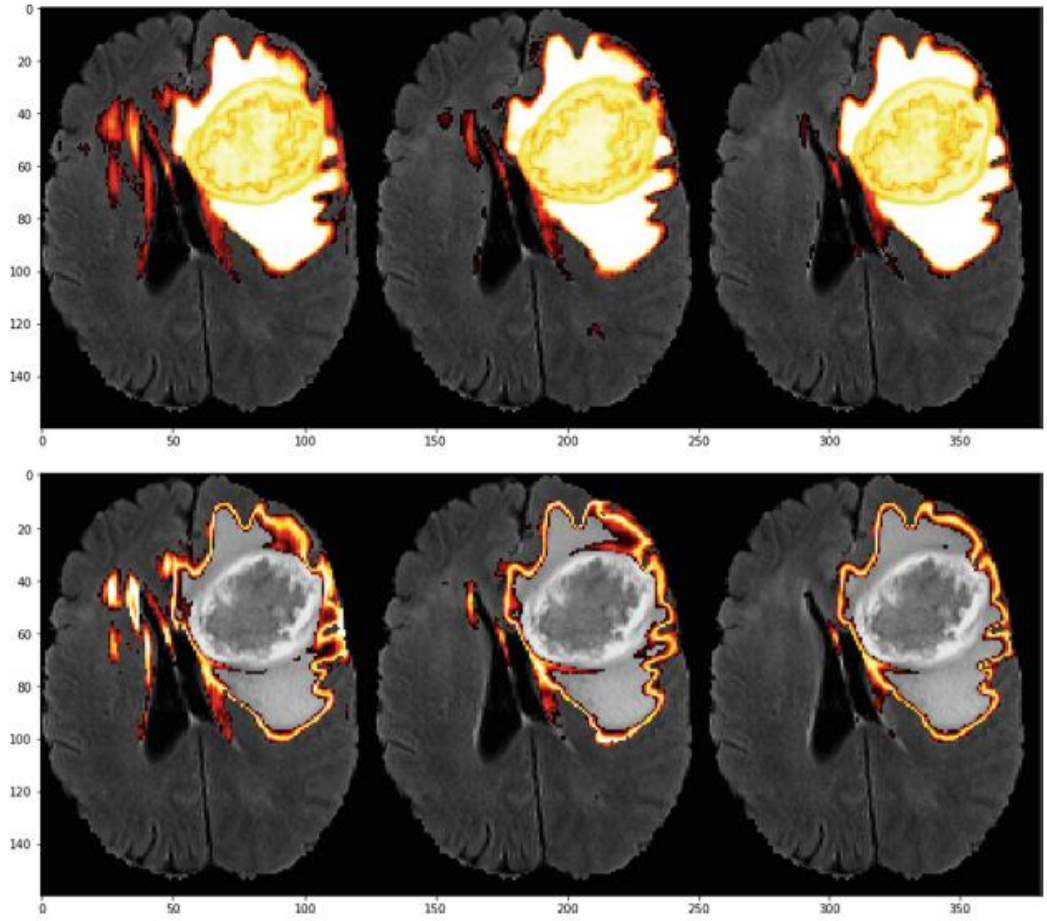

Figure 7. Example segmentation (top row) and prediction uncertainty maps (bottom row) for whole tumour class generated by McKinley et al (2018). From left to right: input provided in sagittal, coronal and axial orientations. The different colors in the top row represent the probability of the whole tumour class (yellow = high probability, red = low probability).

Label	Dice-ET	Dice-WT	Dice-TC	HD95-ET	HD95-WT	HD95-TC
Mean	0.73189	0.88593	0.79926	3.48082	5.5185	5.5347
StdDev	0.27443	0.10182	0.26008	5.52176	9.34294	8.14881
Median	0.83199	0.91786	0.90847	1.73205	3.0	2.82843
25quantile	0.73922	0.87113	0.82327	1.41421	2.23607	1.73205
75quantile	0.88342	0.9396	0.93653	2.82843	5.09902	5.52101

Table 4. Test results achieved by McKinley et al. (2018), sharing 3rd place in the BraTS 2018 challenge. ET stands for enhanced tumour, WT stands for whole tumour and TC stands for tumour core.

On the other hand, Zhou et al. (2018) use an architecture based on FusionNet (Quan et al., 2016), with a U-Net-like structure incorporating residual blocks in both encoder and decoder stages, and utilizing addition skip connections in place of concatenations, see Figures 8 and 9. They further expand their original architecture with a number of modifications, including using a one-pass multi-task structure, a deeper network, dense connections, attention mechanisms, and multi-scale information.

Their networks take as input blocks of size 32x32x16 including all four available MRI modalities and with a batch size of 2, and produce as output predictions for a reduced block of size 20x20x5. The final predictions are obtained by ensembling the predictions from seven different models and applying postprocessing on the result. See Table 5 for some results.

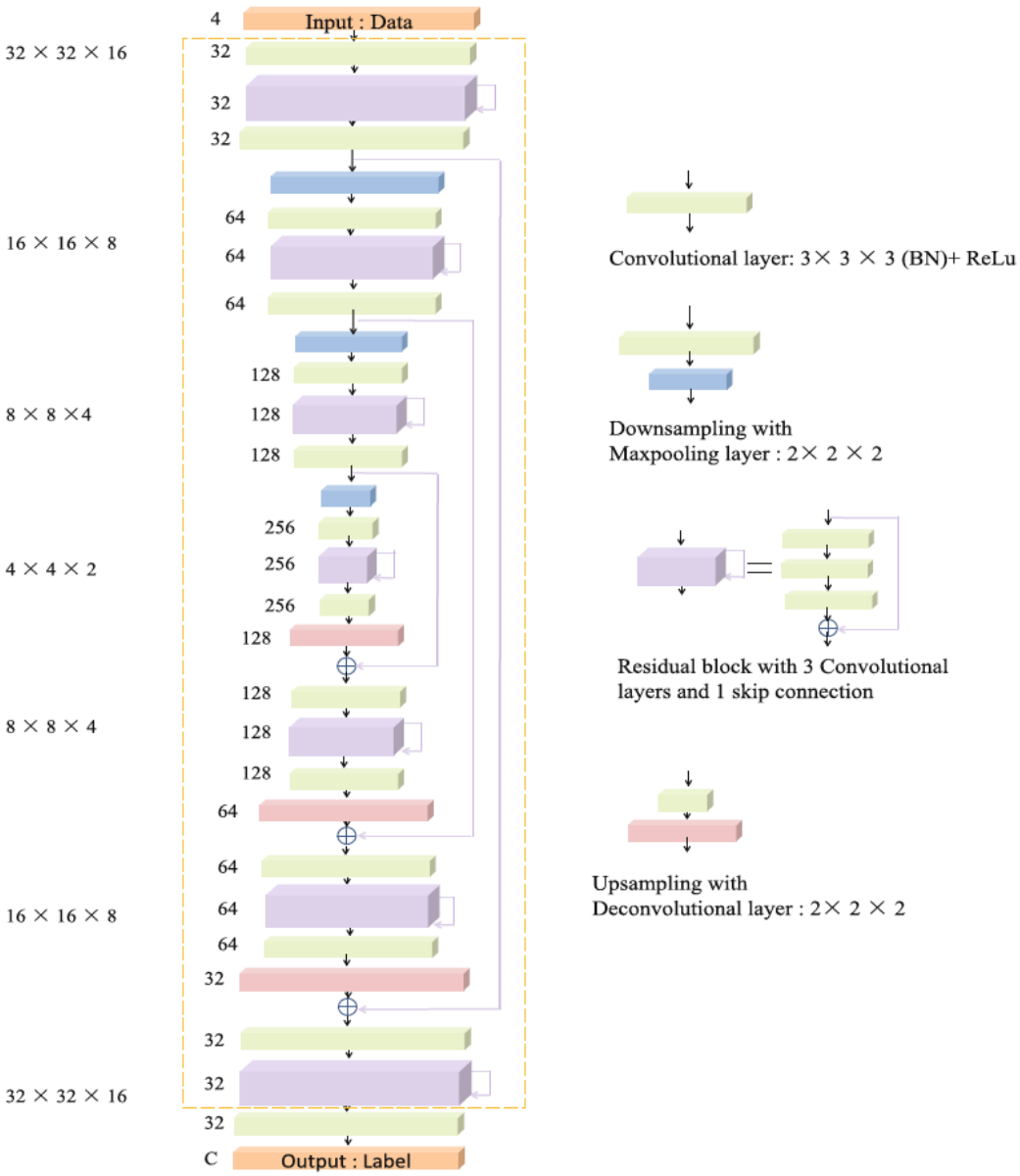

Figure 8. Initial 3D FusionNet architecture employed in Zhou et al. (2018). Three such networks are concatenated to progressively refine the segmentation results. The skip connections are additive instead of concatenations. The region contained in the yellow rectangle constitutes the shared backbone of the one-pass multi-task network.

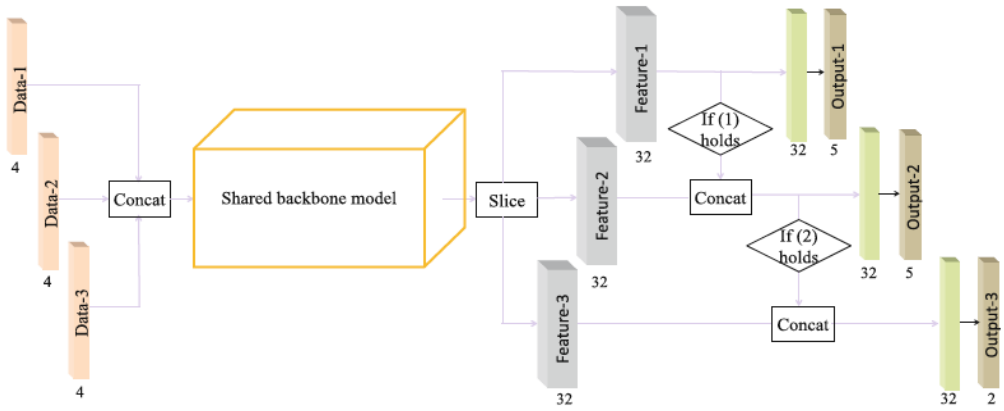

Figure 9. One-pass multi-task network used in Zhou et al. (2018). Only the last layers are particular to the individual classification task, reducing the total number of network weights that need to be learned to provide the final classification.

	Dice			Hausdorff95		
	Enh.	Whole	Core	Enh.	Whole	Core
Mean	0.7775	0.8842	0.7960	2.9366	5.4681	6.8773
StdDev	0.2533	0.1127	0.2593	4.6894	7.6479	10.1779
Median	0.8498	0.9183	0.9030	1.7321	3.1623	3.0000
25quantil	0.7596	0.8725	0.8062	1.4142	2.0000	1.7321
75quantil	0.8997	0.9437	0.9376	2.7337	5.3852	7.2798

Table 5. Test results achieved by Zhou et al. (2018), sharing 3rd place in the BraTS 2018 challenge.

5 Overview of papers focusing on metastases

A large number of papers have used deep learning for detection and segmentation of brain tumours. To use deep learning to detect brain metastases, see Figure 10, is not as common. A possible reason is that there is no openly available MRI dataset specifically containing brain metastases (such as BraTS for brain tumours (Menze et al., 2015)). Collecting MRI brain volumes containing metastases is a more challenging task, since the primary cancer (e.g. lung, breast) needs to spread to the brain. According to a review by Perez et al. (2016), only 10 papers focused specifically on brain metastases, and deep learning was not used in any paper. Liu et al. (2017) trained a 3D CNN based on a modified DeepMedic architecture (Kamnitsas et al. 2017) using data from patients with brain tumours or brain metastases, but only used T1-weighted MR images with contrast and did not report the detection performance (which is crucial, since small metastases are rather easy to miss). Charron et al (2018) also used the DeepMedic architecture, but trained it on multi-modal MRI data, consisting of T1, T1 with contrast and T2 FLAIR, from 182 patients. Manual segmentations were performed by 4 radiology oncologists, which found a total of 412 metastases with a diameter ranging from 1.65 mm to 27 mm. The deep learning approach resulted in a sensitivity of 93% - 98%, with a false positive rate of 4.4 - 14.2 metastases per patient, when tested on 18 patients not used for training. The best single-modality detection performance was obtained with the T1W contrast images, and the performance improved by using all 3 MR modalities. Similar results were obtained by (Grovik et al., 2019), who used a 2.5D, fully convolutional, adaptation of the GoogLeNet architecture to perform the detection using T1, T1 with contrast and T2 FLAIR. It is difficult to compare performance between studies, since no openly available metastasis dataset is available, and a false positive rate of 3 - 5 metastases per patient may be too high for clinical use.

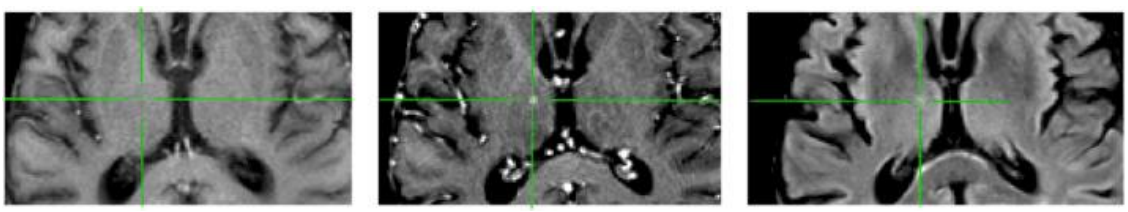

Figure 10. Example of a metastasis shown with T1, T1 Gd contrast and T2 FLAIR (the metastasis is not visible in the native T1 image). Image from (Charron et al., 2018). While metastases are harder to detect than brain tumours, they are easier to treat, for example using the Leksell GammaKnife.

Interestingly, despite acknowledging the lack of data as one of the main shortcomings, these three studies used very little data augmentation. Charron et al. (2018) applied small rotations (< 5 degrees) to generate data representing 62 virtual patients (in addition to the 182 real patients), while Grovik et al. (2019) only applied flips and rotations that are multiples of 90 degrees and Liu et al. (2017) only used flips. A hypothesis is therefore that better performance can be achieved, by for example adding random scalings and elastic deformations. In the original U-Net paper (Ronneberger et al., 2015), elastic deformations were listed as a key feature to train the network with few annotated examples, see Figure 11 for an example.

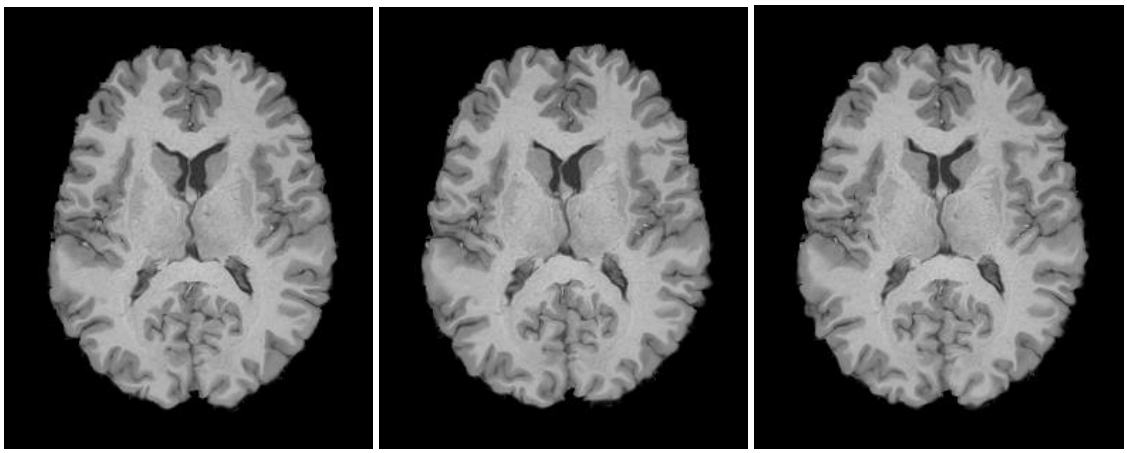

Figure 11. Data augmentation by transforming a brain image with a random smooth displacement field, giving rather realistic augmented brains.

Since there is no openly available dataset with brain metastases, a possible solution is to generate synthetic data, using generative adversarial networks (GANs) (Goodfellow et al., 2014), e.g. to insert brain tumours or brain metastases into MR images from healthy controls. Shin et al. (2018) used such an approach to generate new subjects with brain tumours, see Figure 12. The interesting part is that they took segmented brain tumours from the BraTS dataset (Menze et al., 2015), i.e. the binary masks, and could then change the location or size of the tumour to generate new realistic datasets. Synthetic datasets containing metastases can therefore, at least in theory, be generated by starting from a brain tumour dataset, and make the tumours much smaller. Such a (semi)synthetic dataset can facilitate research about brain metastases, if made openly available. An open research question is if such a dataset can be created from a dataset only containing brain tumours, or if the dataset also needs to contain real brain metastases.

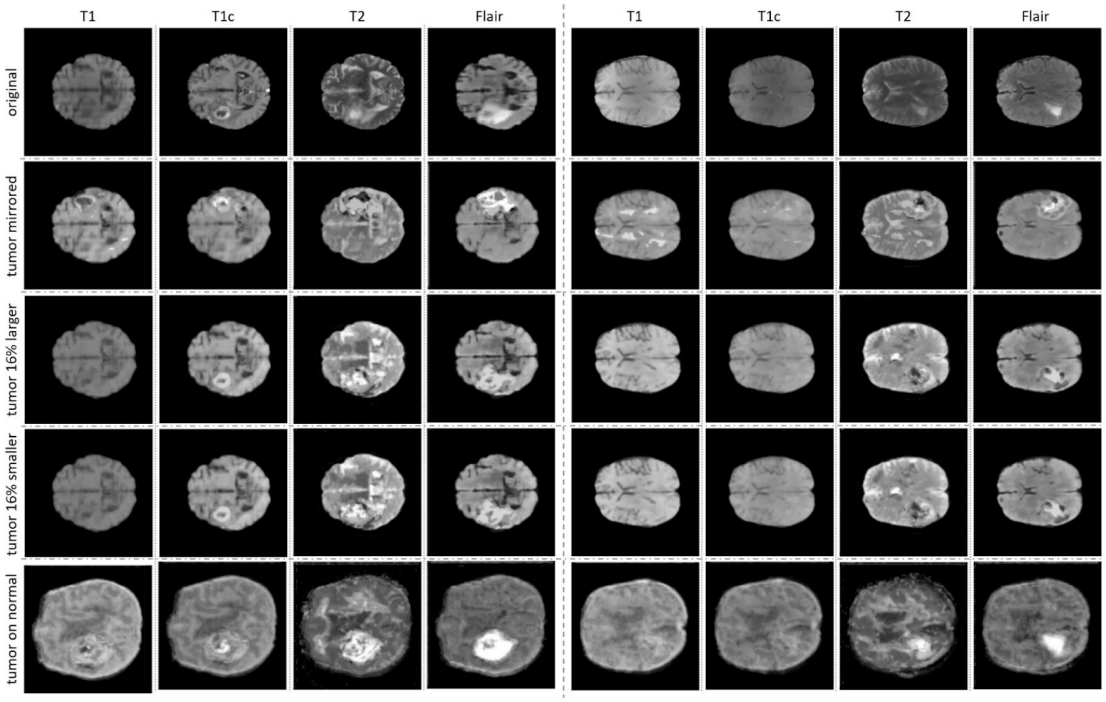

Figure 12. **Top row:** Real images from BraTS dataset. **Second row:** the tumour has been mirrored to the other side of the brain. **Third row:** The tumour has been made 16% larger. **Fourth row:** The tumour has been made 16% smaller. **Fifth row:** A tumour has been added to a subject without tumours. Image from (Shin et al., 2018). Synthetic data with brain metastases can in theory be constructed from the BraTS dataset, by making the tumour labels much smaller.

Krivov and Belyaev (2018) raised another valid question: if detection is such a crucial component of metastasis segmentation, wouldn't it be more natural to split it into two separate steps? In other words, a detection step which proposes suspicious regions for the, possibly computationally expensive, segmentation algorithm to operate on. In computer vision, the task performed by the detection step is referred to as object detection, which has received tremendous attention in recent years (Zou et al., 2019). Another benefit of the two-step approach is that, unlike conventional segmentation, it naturally identifies different metastases as different instances (so called instance segmentation). Incidentally, the current state-of-the-art method for instance segmentation is Mask R-CNN (He et al., 2017).

6 Advanced MRI techniques for improved detection and differentiation of tumour types

Quantitative MRI

The main drawback of T1- and T2-weighted structural MR images is that the intensity values have no physical meaning. This is in contrast to CT (computed tomography), where the intensity values can be interpreted as Hounsfield units. A T1-weighted image collected using MR scanner A can therefore be very different to a T1-weighted image collected using MR scanner B, even if the same subject is scanned twice. A solution to this is to use quantitative MRI (relaxometry), where the actual T1 and T2 relaxation times, and also the proton density, are calculated in each voxel, see Figure 13 for an example. A quantitative MRI sequence for full brain coverage has a scan time of 6 - 7 minutes (Warntjes et al., 2007, 2008). When T1, T2 and PD have been calculated in each voxel, synthetic MR images corresponding to the conventional images can be created for any weighting (e.g. T1- or T2-weighted). In research it is common to work with the relaxation rates R1 and R2, which are defined as R1 = 1/T1 and R2 = 1/T2.

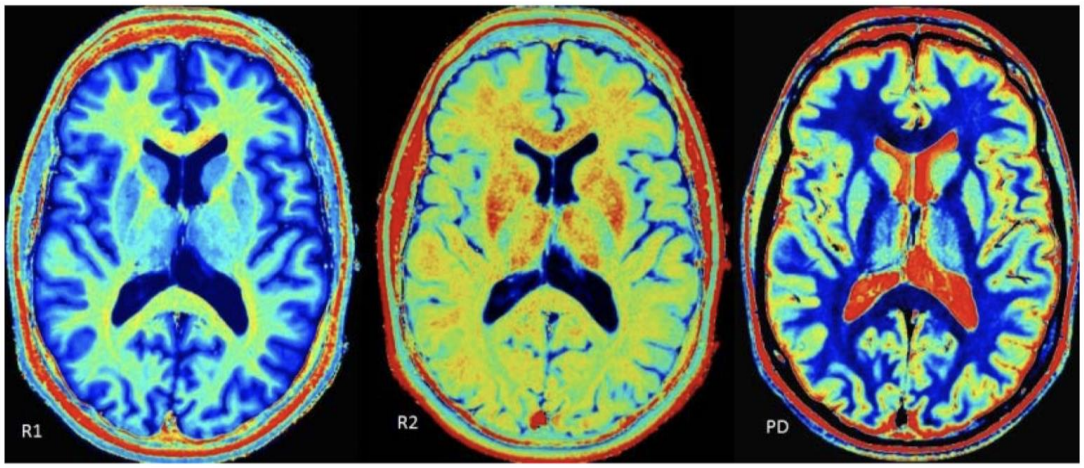

Figure 13. Quantitative maps of the brain, representing R1 (1/T1), R2 (1/T2) and proton density, obtained through a quantitative MRI sequence. Image from (Blystad, 2017).

A major advantage with quantitative values is that it becomes easier to detect and possibly classify abnormal tissue. Different tissue types have different relaxation rates, and normal values for white brain matter (WM), gray brain matter (GM) and cerebrospinal fluid (CSF) are available for comparison. If a voxel has a R1 and/or R2 relaxation rate that is different compared to normal values for WM, GM and CSF, it can be seen as abnormal tissue (e.g. a brain metastasis or a lesion from multiple sclerosis), see Figure 14. From a machine

learning perspective, quantitative values are also beneficial, since it is common that a machine learning algorithm trained on data from scanner A will not perform as well on data from scanner B. Using quantitative data, it is more likely that the algorithm will perform well for both scanners. However, R1, R2 and PD values will differ depending on the field strength of the MR scanner (e.g. 1.5 T or 3 T) and still need to be compensated for (West et al., 2013).

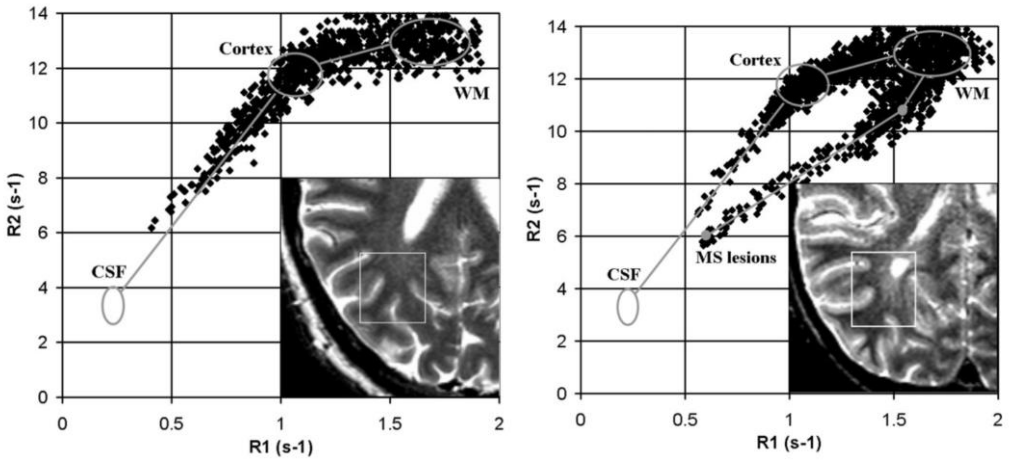

Figure 14. Plots of R1 vs R2 relaxation rates for a healthy control (left) and a patient with multiple sclerosis (MS, right). For the healthy control, the quantitative R1 and R2 values are within the normal range for GM, WM and CSF for all voxels. For the MS patient, some voxels have abnormal R1 and R2 values, which indicate abnormal tissue. Images from (Warntjes et al., 2008).

Gadolinium contrast is normally used when collecting MR images from brain tumour patients, since it will detect contrast agent leakage (damage on the blood-brain-barrier), which makes it easier for the neuroradiologist to detect and to classify the tumour. Leakage of contrast agent will increase R1 in tumour tissue, and a more quantitative definition of the tumour can therefore be obtained by calculating the difference in R1 after and before contrast injection (Blystad et al., 2017) (normally T1-weighted images are collected both before and after contrast injection). This quantitative approach can detect tissue changes in the peritumoral region that are not visible on conventional MR images, see Figure 15, and this information can be useful both for deep learning based segmentation and for planning of radiation therapy.

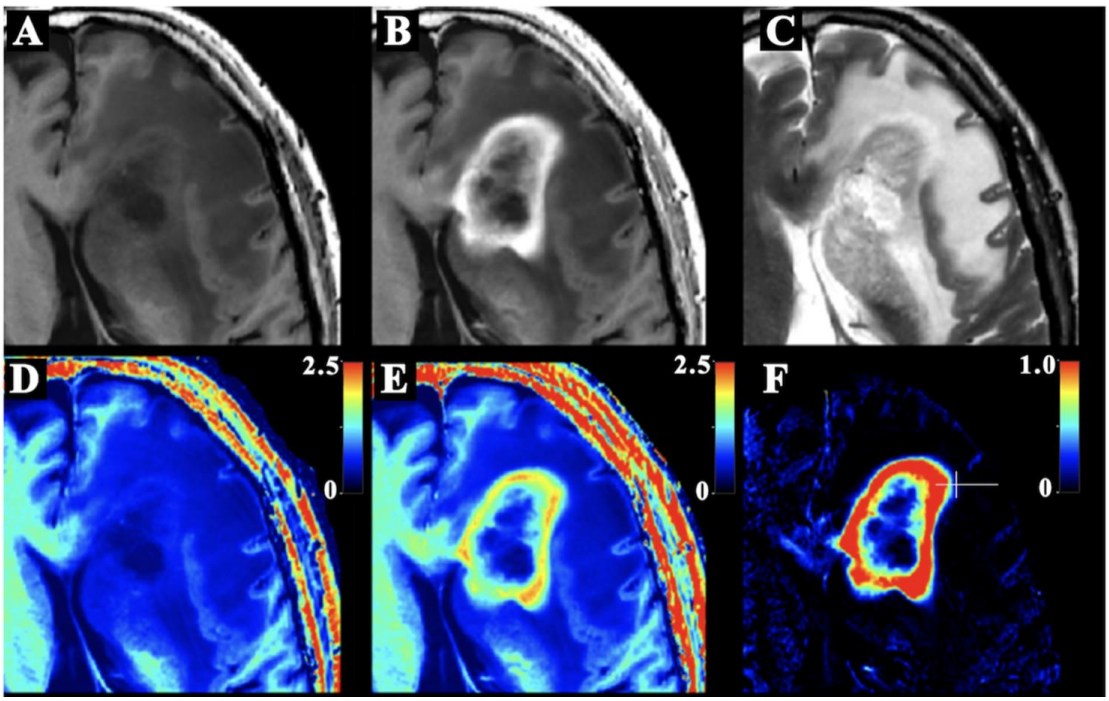

Figure 15. An example of the synthetic and quantitative images of a 76-year-old man with glioblastoma. The top row shows the synthetic images: (A) T1-weighted image without contrast, (B) T1-weighted image after contrast agent injection, (C) T2-weighted image after contrast agent injection. The second row shows the R1 maps: (D) R1 map without contrast agent, (E) R1 after contrast agent injection, (F) difference in R1 maps (small changes in R1 relaxation are due to an imperfect registration). Image from (Blystad et al., 2017).

Hagiwara et al. (2016) applied quantitative MRI to 10 patients with a total of 167 brain metastases, and then produced synthetic MR images with arbitrary weighting. Two radiologists then tried to detect metastases using conventional MR images as well as synthetic MR images. The lesion-to-white matter contrast and contrast-to-noise ratio of the contrast-enhanced synthetic T1 inversion recovery (IR) images were significantly higher than those of the contrast-enhanced synthetic T1W and contrast-enhanced conventional T1IR images. The number of lesions detected by the two neuroradiologists in the synthetic T1IR images was higher than those in the synthetic T1W and conventional T1IR images, but the difference was not statistically significant (which may be explained by the rather low number of patients).

To summarize, the full potential of quantitative MRI has not yet been utilized for detection and segmentation of brain tumours and brain metastases. It would for example be interesting to collect a brain tumour dataset similar to BraTS (Menze et al., 2015), but to add quantitative MRI, calculate R1, R2 and PD maps and compare deep learning performance with and without the quantitative maps.

Diffusion MRI, ADC, DT and other methods

Diffusion MRI (dMRI) is an imaging technique which exploits the random diffusion of water molecules to indirectly probe the microstructure of, for example, biological tissue. One of the discoveries that made dMRI interesting and valuable as a clinical tool was presented by Moseley et al. (1990a). It was shown that diffusion-weighted imaging (DWI) was sensitive tissue disruption in cerebral ischemia in an earlier phase than other imaging techniques (Moseley et al., 1990a, Moseley et al., 1990b). Since then, the field of dMRI has been developing and its clinical use has broadened.

The use of diffusion MRI in the clinical practice is currently limited to the acquisition of diffusion weighted images and the estimation of the Apparent Diffusion Coefficient (ADC) and the Diffusion Tensor (DT) (Basser et al., 1994). Figure 16 shows an example of clinically used images of a brain tumour. The Diffusion Coefficient is the constant relating time and water molecules displacements that one would measure if water was diffusing freely in space. As most biological tissues present some sort of structure that hinders the diffusion process in certain directions, the measured value is generally lower than that for unhindered (free) diffusion, hence the name apparent diffusion coefficient, and it depends on the direction in which the measurement is taken. This method assumes that the diffusion-weighted signal follows a mono-exponential decay given by the expression:

$$S = S_0 \, exp(-b \cdot ADC)$$

where S is the diffusion-weighted signal, S_0 the signal when no diffusion weighting is applied, and b is the b-value.

The diffusion tensor model takes into consideration the fact that water molecules' displacements are not equal in all directions. Diffusion is here represented by a 3x3 symmetric matrix. The diagonal elements of the matrix correspond to diffusivity along three orthogonal axes, while the off-diagonal terms correspond to the correlation along these three orthogonal axes. The signal representation is given by the equation:

$$S = S_0 \, exp(-b : D)$$

where *D* is the diffusion tensor matrix, *b* is a 3x3 symmetric matrix containing the experimental parameters and ":" indicates the scalar product. The diffusion tensors are employed to compute several scalar-valued maps such as, Fractional Anisotropy FA and Mean Diffusivity MD, which are well-suited for group studies.

Many methods other than ADC and DTI have been developed to quantify dMRI data. Among these are: diffusional kurtosis imaging DKI (Jensen et al., 2005), composite hindered and restricted model of diffusion CHARMED (Assaf and Basser, 2005), neurite orientation and density imaging NODDI (Zhang et al., 2012), and mean apparent propagator MRI (Özarslan et al., 2013) to name a few. According to (Novikov et al., 2018), these methods are classified into two broad categories named “signal representations” and “biophysical models”. Methods belonging to the first category, such as e.g. DTI and DKI, provide descriptive statistics of the diffusion process, and make few assumptions about the tissue compositions. Even though these methods’ purpose is not to infer any particular aspect of the tissue microstructure, there exist many studies linking parameters derived from them to tumour tissue features and have a potential use as imaging biomarkers. Methods belonging to the second category are instead constructed with the aim of estimating explicit microstructures features and therefore offer a more direct instrument to probe the tumours’ microstructure. However, their use in brain tumours imaging is still limited (Nilsson et al., 2018).

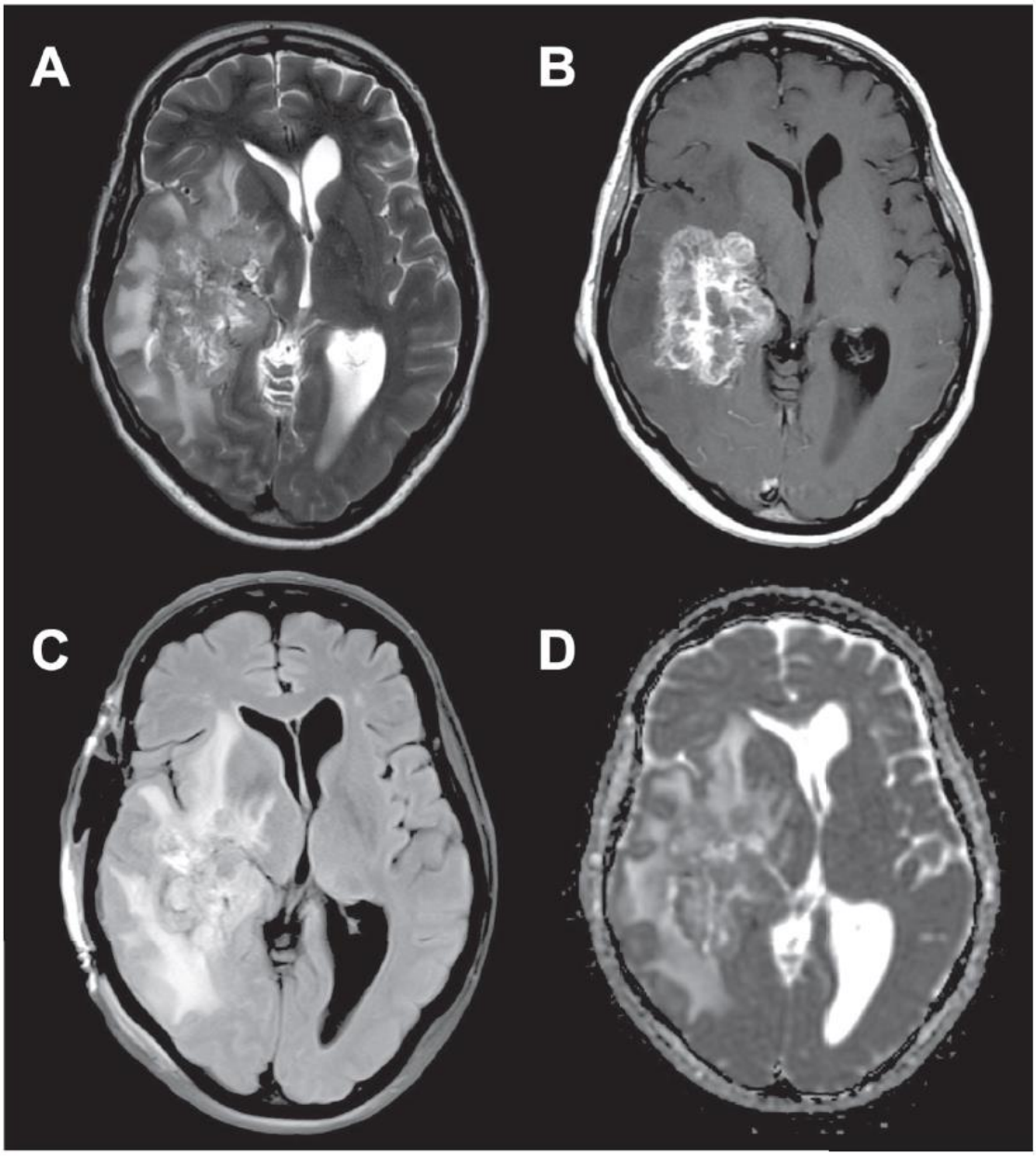

Figure 16. Clinical MRI of a grade IV glioblastoma. (A) T2 Weighted image, (B) Gadolinium enhanced T1 Weighted image, (C) FLAIR image, (D) ADC map. Figure retrieved from (Nilsson et al., 2018).

Current clinical practice in brain tumour imaging and challenges

ADC

As previously mentioned, the use of dMRI in the clinics is currently limited to the acquisition of diffusion weighted images and the computation of the ADC, DT and DT derived parameters. Examples on how these information are employed in brain tumour treatment can be found in (Villanueva-Meyer et al., 2017) and (Nilsson et al., 2018). In these reviews it was reported that DWI is best used to characterize tumour cellularity. Several studies have confirmed that low ADC values are found to be related to highly cellular tumours such as lymphoma and medulloblastoma. However, contradictory findings were reported for example by Jenkinson et al., (2009) and Sadeghi et al., (2008). The reason behind these findings was that mechanisms other than cellularity are known to influence the ADC. Thus, more advanced methods are required to disentangle the different contributions.

The ADC has also been used for monitoring treatment and tumour differentiation. Treatment monitoring uses the fact that ADC values react to the lowering in tumour cellularity due to cell lysis within few days or weeks after the treatment has started. However, Morse et al., (2007) reported that the relationship between cell apoptosis and ADC response can be complex. This makes the conclusions based on ADC values unreliable. Moffat et al. (2005) and Galbán et al. (2009) proposed a solution to these problems using an approach referred to as functional diffusional map fDM or parametric response map PRM. Here post-treatment parameters are registered to pre-treatment parameters, and the fractional volume of positive and negative change in ADC is computed. Indications of successful treatment were found in cases where large volumes presented an increase in ADC. Figure 17 shows how the parametric map is created and what it displays.

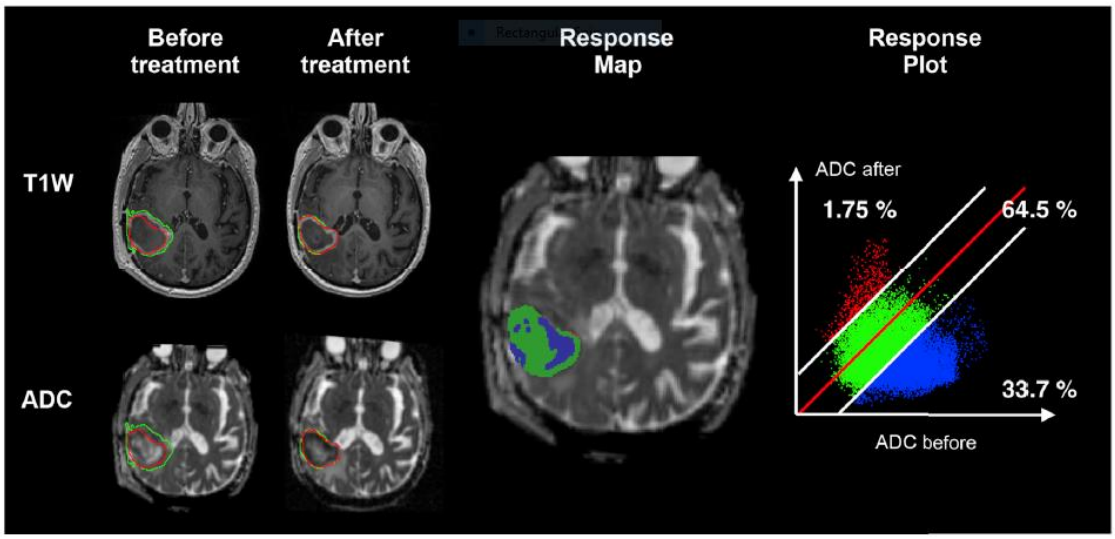

Figure 17. Parametric Response Mapping. An MRI exam is performed before and after the treatment and the volumes are coregistered. The response map is computed on the ADC: the green colour represents areas where there was no substantial change in ADC value, blue represents a substantial decrease in ADC value and red an increase in ADC value. The fractional volume of ADC increase or decrease can be used to assess the response to the cure within weeks after treatment initiation (Moffat et al., 2005). Figure retrieved from (Nilsson et al., 2018).

Tumour differentiation is often based on ADC values only as reported in Yamasaki et al., 2005. It can also be used to differentiate between different subgroups, although studies such as (Sanverdi et al., 2012) reported that ADC values were not useful in differentiating between different subtypes of Meningioma.

The use of ADC values is also found in the assessment of tumour grade and in the localization of tumour infiltrated foci among regions of vasogenic oedema (Villanueva-Meyer et al., 2017). However, as the authors reported, the overlap in ADC values between tumour grades limits the role of quantitative ADC in clinical practice.

DTI

Villanueva-Meyer et al., (2017) and Nilsson et al. (2018) reviewed the use of DTI as a tool for presurgical planning. DTI-based tractography is reported to be used to assess the integrity of white matter fibers and to guide the surgical resection of the tumour, see Figure 18. However, DTI presents the severe limitation of being able to resolve a single fiber direction per voxel, becoming extremely inaccurate in case of multiple fiber directions. Methods using higher angular resolution data and multiple b-values, see (Tournier et el., 2011) for a complete overview, have been introduced with the purpose of overcoming this

limitation but have not yet been adopted in the clinical context due to the complex data acquisition scheme.

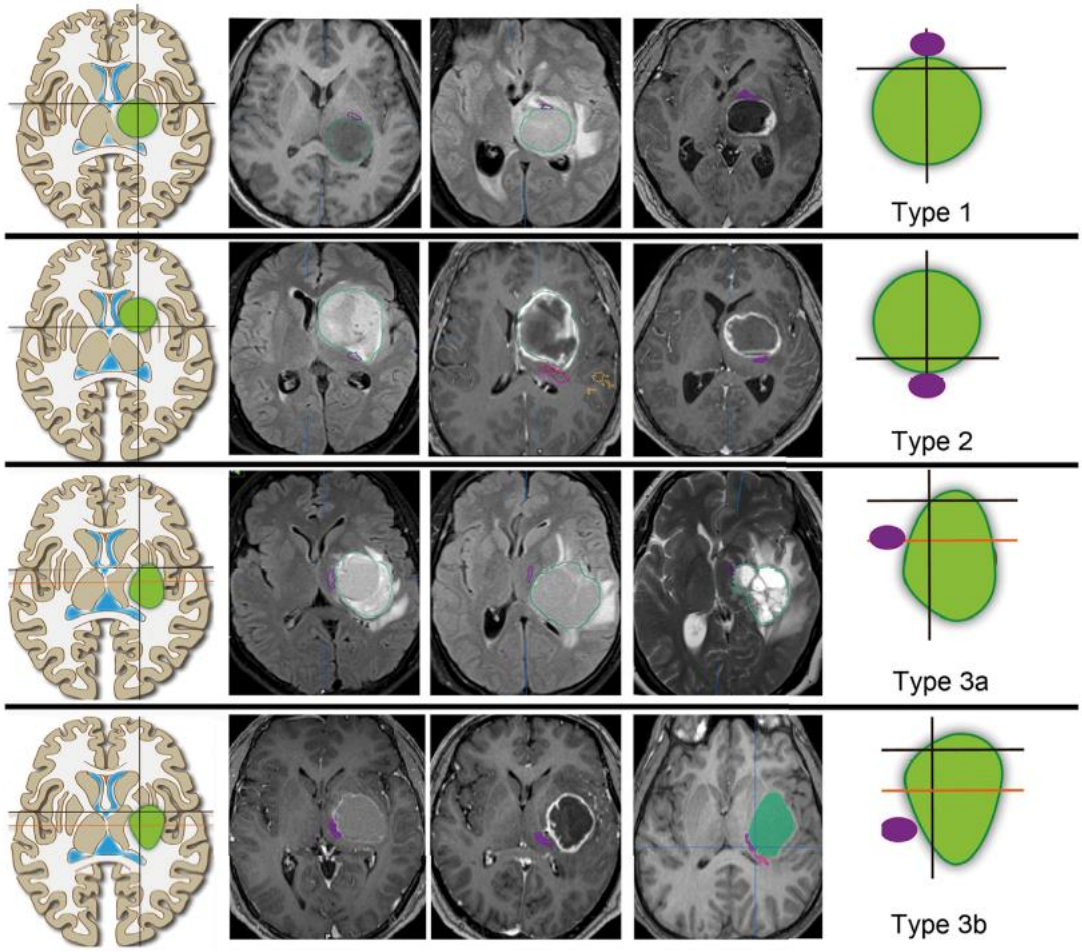

Figure 18. Examples of pre-surgical tractography for thalamic or basal ganglia tumours. This kind of analysis shows how to locate fiber tracts (the pyramidal tract in these examples) before performing tumour resection. The left column shows the tumour location types. The right column depicts the relative positions of the dislocated pyramidal tract. Green circles indicate tumours and purple circles indicate the pyramidal tract location. The middle three columns illustrate typical scenarios. Figure reproduced from (Hou et al., 2012).

DKI

Diffusional Kurtosis Imaging (Jensen et al., 2005) is the extension of DTI to the analysis of data collected at both low and high b-values. The signal representation in one dimension is given by the following expression:

$$S = S_0 exp(-b\,MD + \tfrac{1}{6}b^2\,MD\,MK)$$

where MK represents the mean kurtosis which is the amount by which the signal departs from the mono-exponential decay. DKI has been applied in tumour grading. A meta-analysis from Delgado et al., 2018 revealed that DKI has high diagnostic accuracy in differentiating between low- and high-grade Gliomas. Increasing values of MK have been reported to correlate with increasing tumour grade (Raja et al., 2016; Van Cauter et al., 2012) while others showed that this relation is not always useful in differentiating, for example, Gliomas of grade II and III (Delgado et al., 2017).

Diffusion encoding with general gradient waveforms and its potential utility in examining brain tumours

As summarised above, dMRI methods currently used in the clinical practice present significant limitations. As already mentioned, the ADC value depends on the direction along which the measurement is taken. Moreover, it only provides an average of all the ADCs across a voxel. For what concerns DTI, Jones et al., (2012) contains a comprehensive guide on its limitations and how the results should be interpreted in the light of those limitations. One limitation is of particular interest for this report, and is the fact that the diffusion tensor fails in capturing intravoxel diffusion heterogeneity, i.e., multiple diffusion rates within one voxel. The diffusion tensor only retains an average of the diffusivity across the whole voxel, and thus cannot provide an accurate description of the tissue heterogeneity.

To overcome such limitations, techniques sensitive to the local (microscopic) anisotropy of the specimen could be employed. A natural extension of standard diffusion encoding, which employs one pair of diffusion gradients is double diffusion encoding (DDE or dPFG), which was shown to be sensitive to anisotropy at different length scales (Cheng and Cory, 1999; Özarslan and Basser, 2008; Özarslan, 2009). A further extension to completely general gradient waveforms has resulted in the development of q-space trajectory imaging (QTI) (Westin et al., 2016), which is potentially able to resolve multiple cell shape, size and orientation within one voxel. The QTI framework consists of two components, encoding and modelling. Encoding is performed by

employment of general gradient waveforms as opposed to the sequence designed by Stejskal and Tanner comprising a single pair of pulsed gradients. The b-value found in the previous equations is here extended to a tensor entity referred to as the b-tensor. Modelling is done by adopting the diffusion tensor distribution model introduced by Jian et al., (2007) in each voxel. Such framework provides a description of the tissue microstructure which is not achievable with conventional methods where information such as variance in microscopic anisotropy and isotropic diffusivity are entangled.

Following the idea of encoding the signal using different b-tensor shapes, Szczepankiewicz et al., (2016) introduced a method called diffusional variance decomposition (DIVIDE) and used it to analyse the tissue microstructure of Gliomas and Meningiomas. The DIVIDE method uses two different shapes of the b-tensor, linear and spherical. With this approach it is possible to separate the total kurtosis MK_T (which in this method is referred to as diffusional variance) into its anisotropic MK_A and isotropic MK_I components. The total kurtosis constitutes an indicator of tissue heterogeneity, i.e., the higher its value the higher the heterogeneity within the tissue. MK_A and MK_I can be used to determine the type of heterogeneity, whether it is due to anisotropic compartments with orientation dispersion (MK_A) or intra-voxel variance in isotropic diffusivity (MK_I). The results of the paper highlighted how MK_T was high in both types of tumour, indicating heterogeneity in the tissues, and how the source of this heterogeneity could be determined using the anisotropic and isotropic diffusional variance. The Meningioma was characterized by high MK_A, indicating high variance in cell eccentricity, while the glioma was characterized by high MK_I, indicating high variance in cell density, see Figure 19. The results were confirmed by quantitative microscopy on the resected tumours, Figure 20.

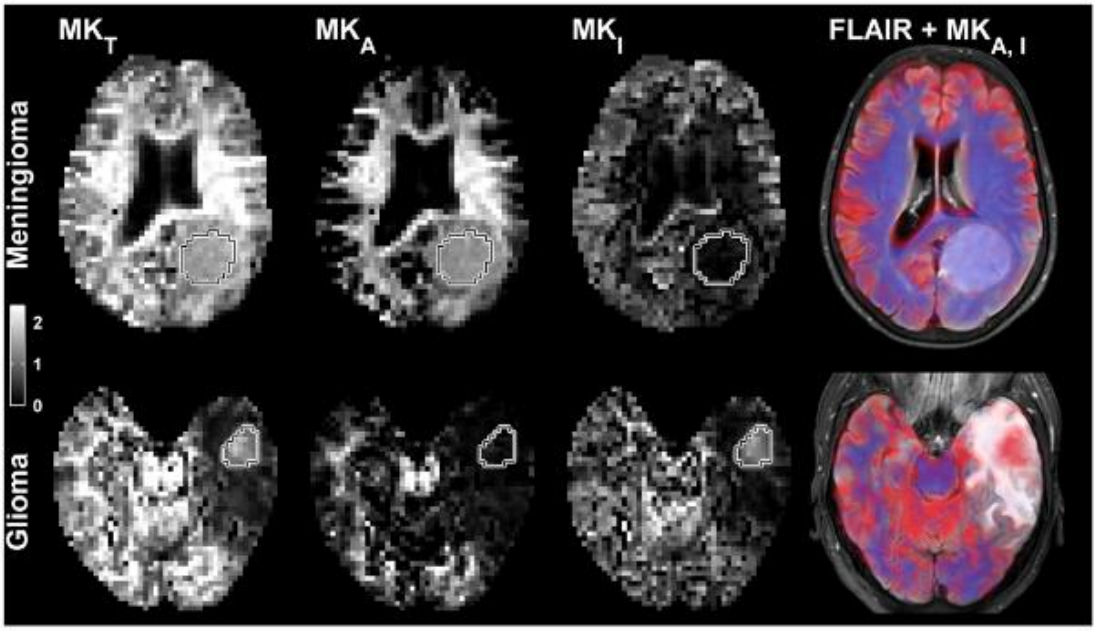

Figure 19. Examples of maps of DIVIDE parameters on brains with Meningioma and glioma. MK_T is high in both tumour types while MK_A and MK_I exhibit different behaviour in the two cases. On the last column on the right, $MK_{A,I}$ were superimposed on a high resolution morphological fluid-attenuated inversion recovery (FLAIR) image. MK_A was color-coded in blue and MK_I was color-coded in red. The Meningioma presented high MK_A and low MK_I while the opposite was found in the Glioma. Figure retrieved from (Szczepankiewicz et al., 2016).

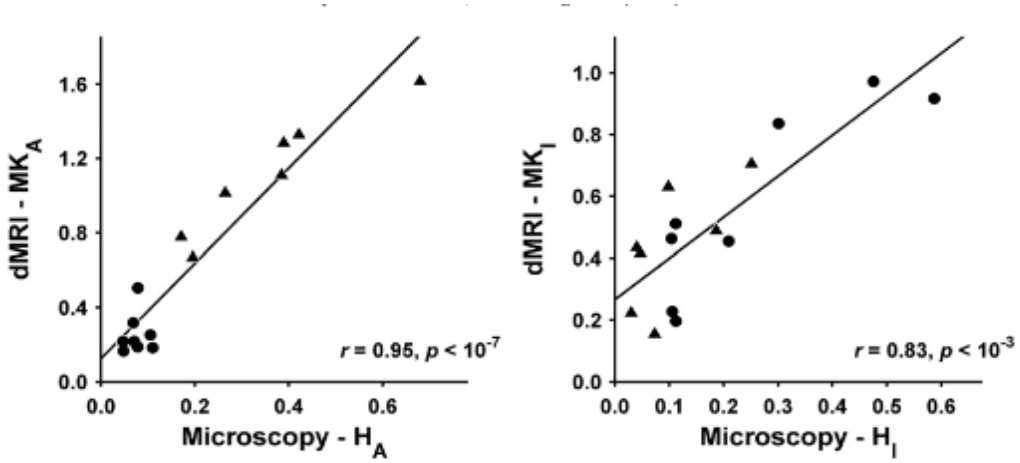

Figure 20. Correlation between variance parameters derived from dMRI and microscopy in Meningiomas (triangles) and Gliomas (circles). The anisotropic and isotropic components MK_A and MK_I present strong positive correlations to structural anisotropy H_A and cell density variance H_I, respectively. H_A was derived from a structure tensor analysis while H_I was obtained from cell nuclei segmentation. Figure retrieved from (Szczepankiewicz et al., 2016).

7 Concluding remarks

To conclude, a large body of research has used deep learning for detection and segmentation of brain tumours, but little work has focused on brain metastases. A possible reason for this is the lack of an open dataset specifically containing (small) brain metastases. Virtually all the deep learning based approaches have used structural MRI for the segmentation, and an hypothesis is that also including quantitative MRI and diffusion MRI can further improve the segmentation. For CNNs, this can be achieved rather easily, by for example increasing the number of channels from 4 (T1W, T1W after contrast, T2W, FLAIR) to 8 (adding channels for T1 relaxation rate, T2 relaxation rate, proton density, and fractional anisotropy from diffusion MR). One problem of combining different types of MRI data is that diffusion MRI data often have a lower spatial resolution (e.g. 2 x 2 x 2 mm) compared to structural MRI (e.g. 1 x 1 x 1 mm). This can be solved in different ways, such as upsampling the diffusion MRI data or having several paths in the CNN. Another problem with diffusion MRI is that the data have rather strong distortions which need to be corrected for.

An MRI modality not covered in this state of the art report is MR elastography (MRE), which can measure tissue stiffness non-invasively (Di leva et al., 2010). Since tumour tissue often has a different stiffness compared to healthy tissue, MRE can be used for tumour detection. However, MRE requires additional hardware (a wave driver to generate mechanical excitation) and MRE is therefore not as common as structural MRI.

8 References

Apra, C, Peyre, M, Kalamarides, M. (2018). Current treatment options for meningioma, Expert Review of Neurotherapeutics, Expert Reviews (formerly Future Drugs), 18 (3), 241- 249.

Assaf, Y., Basser, P.J., 2005. Composite hindered and restricted model of diffusion (CHARMED) MR imaging of the human brain. NeuroImage. 27, 48–58.

Basser, P. J., Mattiello, J. & Le Bihan, D. 1994. MR diffusion tensor spectroscopy and imaging. *Biophysical Journal,* 66, 259-67.

Blystad, I., Clinical Applications of Synthetic MRI of the Brain, Linköping University Medical Dissertations No. 1600, 2017,
http://liu.diva-portal.org/smash/get/diva2:1157593/FULLTEXT01.pdf

Blystad, I., Warntjes, J. M., Smedby, Ö., Lundberg, P., Larsson, E. M., & Tisell, A. (2017). Quantitative MRI for analysis of peritumoral edema in malignant gliomas. *PLoS One*, *12*(5), e0177135.

Brown, P. D., Ahluwalia, M. S., Khan, O. H., Asher, A. L., Wefel, J. S., Gondi, V. (2017), Whole-Brain Radiotherapy for Brain Metastases: Evolution or Revolution?, *J Clin Oncol*., 36(5):483–491.

Brown, P. D., Jaeckle, K., Ballman, K. V., et al. (2016). Effect of Radiosurgery Alone vs Radiosurgery With Whole Brain Radiation Therapy on Cognitive Function in Patients With 1 to 3 Brain Metastases: A Randomized Clinical Trial [published correction appears in JAMA. 2018 Aug 7;320(5):510]. *JAMA*, 316(4), 401–409.

Charron, O., Lallement, A., Jarnet, D., Noblet, V., Clavier, J. B., & Meyer, P. (2018). Automatic detection and segmentation of brain metastases on multimodal MR images with a deep convolutional neural network. *Computers in biology and medicine*, *95*, 43-54.

Cheng, Y., Cory, D.G., 1999. Multiple scattering by NMR, *J. Am. Chem. Soc.* 121, 7935–7936.

Curado, M. P., Edwards, B., Shin, H. R., et al. (2007). IARC Scientific Publications. Vol. 160. Lyon France: 2007. Cancer Incidence in Five Countries Volume IX.

Delgado, A.F., Fahlström, M., Nilsson, M., 2017. Diffusion kurtosis imaging of Gliomas grades II and III-a study of perilesional tumor infiltration, tumor grades and subtypes at clinical presentation. *Radiology*. 51, 121-129

Di Ieva, A., Grizzi, F., Rognone, E., Tse, Z. T. H., Parittotokkaporn, T., y Baena, F. R., ... & Baena, R. R. (2010). Magnetic resonance elastography: a general overview of its current and future applications in brain imaging. *Neurosurgical review*, *33*(2), 137-145.

Di Lorenzo, R., Ahluwalia, M. S. (2017). Targeted therapy of brain metastases: latest evidence and clinical implications. *Ther Adv Med Oncol*., 9(12), 781–796

Galban, C.J., Chenevert, T.L., Meyer, C.R., Tsien, C., Lawrence, T.S., Hamstra, D.A., Junck, L., Sundgren, P.C., Johnson, T.D., Ross, D.J., Rehemtulla, A., Ross, B.D., 2009. The parametric response map is an imaging biomarker for early cancer treatment outcome. *Nature Medicine.* 15, 572–576.

Goodenberger, M. L., Jenkins, R. B. (2012). Genetics of adult glioma, Cancer Genetics, 205(12),613 - 621

Goodfellow, I., Pouget-Abadie, J., Mirza, M., Xu, B., Warde-Farley, D., Ozair, S., ... & Bengio, Y, Generative adversarial nets. In *Advances in neural information processing systems*, pp. 2672-2680, 2014

Grøvik, E. , Yi, D. , Iv, M. , Tong, E. , Rubin, D. and Zaharchuk, G. (2019), Deep learning enables automatic detection and segmentation of brain metastases on multisequence MRI. J Magn Reson Imaging. doi:10.1002/jmri.26766

Hagiwara, A., Hori, M., Suzuki, M., Andica, C., Nakazawa, M., Tsuruta, K., ... & Kumamaru, K. K. (2016). Contrast-enhanced synthetic MRI for the detection of brain metastases. *Acta radiologica open*, *5*(2), 2058460115626757.

He, K., Gkioxari, G., Dollár, P. and Girshick, R., 2017. Mask R-CNN. In *Proceedings of the IEEE international conference on computer vision* (pp. 2961-2969).

Hou Y., Chen X., Xu B. 2012. Prediction of the Location of the Pyramidal Tract in Patients with Thalamic or Basal Ganglia Tumors. PLoS ONE 7(11): e48585. https://doi.org/10.1371/journal.pone.0048585

Iacob, G., Dinca, E. B. (2009). Current data and strategy in glioblastoma multiforme, J Med Life., 2(386).

Isensee, Fabian, et al. "No new-net." *International MICCAI Brainlesion Workshop*. Springer, Cham, 2018.

Jensen, J.H., Helpern, J.A., Ramani, A., Lu, H., Kaczynski, K., 2005. Diffusional kurtosis imaging: the quantification of non-Gaussian water diffusion by means of magnetic resonance imaging. *Magnetic Resonance in Medicine*. 53, 1432–1440.

Jenkinson, M.D., Plessis, du, D.G., Smith, T.S., Brodbelt, A.R., Joyce, K.A., Walker, C., 2009. Cellularity and apparent diffusion coefficient in oligodendroglial tumours characterized by genotype. *Journal of Neuro-oncology*. 96, 385–392.

Jian, B., Vemuri, B. C., Özarslan, E., Carney, P. R. & Mareci, T. H. 2007. A novel tensor distribution model for the diffusion-weighted MR signal. *NeuroImage,* 37(1), 164–176.

Jones, D.K., Knösche, T.R., Turner, R., 2012. White matter integrity, fiber count, and other fallacies: the do's and don'ts of diffusion MRI. *NeuroImage.* 73, 239-54

Kamnitsas, Konstantinos, et al. "Ensembles of multiple models and architectures for robust brain tumour segmentation." *International MICCAI Brainlesion Workshop*. Springer, Cham, 2017.

Koshy, M., Villano, J., L., Dolecek, T. A., Howard, A., Mahmood, U., Chmura, S. J. (2012). Improved survival time trends for glioblastoma using the SEER 17 population-based registries. J Neurooncol. 107(207)

Krivov, E. and Belyaev, M. (2018). It doesn't take a whole U-Net to find brain tumors: towards fast brain metastasis segmentation with sparse predictions, *1st Conference on Medical Imaging with Deep Learning (MIDL 2018)*.

Le Rhun, E., Taillibert, S. and Chamberlain, M. C. (2016). Systemic therapy for recurrent meningioma, Expert Review of Neurotherapeutics, 16(8), 889-901

Liu, Y., Stojadinovic, S., Hrycushko, B., Wardak, Z., Lau, S., Lu, W., ... & Nedzi, L. (2017). A deep convolutional neural network-based automatic delineation strategy for multiple brain metastases stereotactic radiosurgery. *PloS one*, *12*(10), e0185844.

McKinley, Richard, Raphael Meier, and Roland Wiest. "Ensembles of densely-connected CNNs with label-uncertainty for brain tumor segmentation." *International MICCAI Brainlesion Workshop*. Springer, Cham, 2018.

Melmed, S. (2011). Pathogenesis of pituitary tumors, Nature Reviews Endocrinology, 7, 257-266

Menze, B. H., Jakab, A., Bauer, S., Kalpathy-Cramer, J., Farahani, K., Kirby, J., ... & Lanczi, L. (2015). The multimodal brain tumor image segmentation benchmark (BRATS). *IEEE transactions on medical imaging*, *34*(10), 1993-2024

Moffat, B.A., Chenevert, T.L., Lawrence, T.S., Meyer, C.R., Johnson, T.D., Dong, Q., Tsien, C., Mukherji, S., Quint, D.J., Gebarski, S.S., Robertson, P.L., Junck, L.R., Rehemtulla, A., Ross, B.D., 2005. Functional diffusion map: a noninvasive MRI biomarker for early stratification of clinical brain tumor response. *Proceedings of National Academy of Science U.S.A.* 102, 5524–5529.

Molitch, M. E. (2016). Diagnosis and Treatment of Pituitary Adenomas: A Review. *JAMA,* 317(5), 516–524.

Morse, D.L., Galons, J.-P., Payne, C.M., Jennings, D.L., Day, S., Xia, G., Gillies, R.J., 2007. MRI-measured water mobility increases in response to chemotherapy via multiple cell-death mechanisms. *NMR Biomedicine* 20, 602–614.

Moseley, M. E., Cohen, Y., Mintorovitch, J., Chileuitt, L., Shimizu, H., Kucharczyk, J., Wendland, M. F. & Weinstein, P. R. 1990a. Early detection of regional cerebral ischemia in cats: comparison of diffusion- and T2-weighted MRI and spectroscopy. *Magnetic Resonance in Medicine,* 14, 330-46.

Moseley, M. E., Kucharczyk, J., Mintorovitch, J., Cohen, Y., Kurhanewicz, J., Derugin, N., Asgari, H. & Norman, D. 1990b. Diffusion-weighted MR imaging of acute stroke: correlation with T2-weighted and magnetic susceptibility-enhanced MR imaging in cats. *AJNR: American Journal of Neuroradiology,* 11, 423-9.

Myronenko, Andriy. "3D MRI brain tumor segmentation using autoencoder regularization." *International MICCAI Brainlesion Workshop*. Springer, Cham, 2018.

Nillson, M., Englund, E., Szczepankiewicz, F., van Westen, D., Sundgren, P.C. 2018. Imaging Brain Tumour Microstructure. *NeuroImage,* 182, 232-250.

Novikov, D.S., Kiselev, V.G., Jespersen, S.N., 2018. On modeling. *Magnetic Resonance in Medicine* 79,3172–3193.

Paolillo M, Boselli C, Schinelli S.(2018). Glioblastoma under Siege: An Overview of Current Therapeutic Strategies. *Brain Sci*., 8(1):15

Perez, U., Arana, E., & Moratal, D. (2016). Brain metastases detection algorithms in magnetic resonance imaging. *IEEE Latin America Transactions*, *14*(3), 1109-1114.

Quan, Tran Minh, David GC Hildebrand, and Won-Ki Jeong. "Fusionnet: A deep fully residual convolutional neural network for image segmentation in connectomics." *arXiv preprint arXiv:1612.05360* (2016).

Ostrom, Q. T., Gittleman, H., Truitt, G., Boscia, A., Kruchko, C., Barnholtz-Sloan, J. S. (2018). CBTRUS Statistical Report: Primary Brain and Other Central Nervous System Tumors Diagnosed in the United States in 2011–2015, *Neuro-Oncology*, 20(suppl_4),iv1–iv86,

Raja, R., Sinha, N., Saini, J., Mahadevan, A., Rao, K.N., Swaminathan, A., 2016. Assessment of tissue heterogeneity using diffusion tensor and diffusion kurtosis imaging for grading Gliomas. *Neuroradiology*. 58, 1217–1231.

Ronneberger, O., Fischer, P., & Brox, T. . U-net: Convolutional networks for biomedical image segmentation. In *International Conference on Medical image computing and computer-assisted intervention (MICCAI),* pp. 234-241, (2015)

Sadeghi, N., D'Haene, N., Decaestecker, C., Levivier, M., Metens, T., Maris, C., Wikler, D., Baleriaux, D., Salmon, I., Goldman, S., 2008. Apparent diffusion coefficient and cerebral blood volume in brain Gliomas: relation to tumor cell density and tumor microvessel density based on stereotactic biopsies. *American Journal of Neuroradiology*. 29, 476–482.

Sanverdi, S. E., Ozgen, B., Oguz, K. K., Mut, M., Dolgun, A., Soylemezoglu, F. & Cila, A. 2012. Is diffusion-weighted imaging useful in grading and differentiating histopathological subtypes of Meningiomas? *European Journal of Radiology,* 81, 2389-95.

Sahgal, A., Ruschin, M., Ma, L., Verbakel, W., Larson, D., Brown, P. D. (2017). Stereotactic radiosurgery alone for multiple brain metastases? A review of clinical and technical issues. *Neuro Oncol*., 19(suppl_2), ii2–ii15.

Shin, H. C., Tenenholtz, N. A., Rogers, J. K., Schwarz, C. G., Senjem, M. L., Gunter, J. L., ... & Michalski, M. (2018). Medical image synthesis for data augmentation and anonymization using generative adversarial networks. In *International Workshop on Simulation and Synthesis in Medical Imaging* (pp. 1-11). Springer, Cham.

Szczepankiewicz, F., van Westen, D., Englund, E., Westin, C.-F., Ståhlberg, F., Lätt, J., Sundgren, P.C., Nilsson, M., 2016. The link between diffusion MRI and tumor heterogeneity: mapping cell eccentricity and density by diffusional variance decomposition (DIVIDE). *NeuroImage*. 142, 522–532.

Tournier, J.-D., Mori, S., Leemans, A., 2011. Diffusion tensor imaging and beyond. *Magnetic Resonance in Medicine*. 65, 1532–1556.

Tsao, M. N., Sahgal, A., Xu, W., et al. (2017), Stereotactic radiosurgery for vestibular schwannoma: International Stereotactic Radiosurgery Society (ISRS) Practice Guideline. *J Radiosurg SBRT*, 5(1), 5–24.

Van Cauter, S., Veraart, J., Sijbers, J., Peeters, R.R., Himmelreich, U., De Keyzer, F., Van Gool, S.W., Van Calenbergh, F., De Vleeschouwer, S., Van Hecke, W., Sunaert, S., 2012. Gliomas: diffusion kurtosis MR imaging in grading. *Radiology*. 263, 492–501.

Villanueva-Meyer, J.E., Mabray M. C, Cha S. 2017. Current Clinical Brain Tumour Imaging. *Neurosurgery,* 81, 397-415

Wang, Guotai, et al. "Automatic brain tumor segmentation using cascaded anisotropic convolutional neural networks." *International MICCAI Brainlesion Workshop*. Springer, Cham, 2017.

Warntjes JB, Leinhard OD, West J, Lundberg P. Rapid magnetic resonance quantification on the brain: Optimization for clinical usage. Magn Reson Med. 2008 Aug;60(2):320–9

Warntjes JB, Dahlqvist O, Lundberg P. Novel method for rapid, simultaneous T1, T*2, and proton density quantification. Magn Reson Med. 2007 Mar;57(3):528–37

West, J., Blystad, I., Engström, M., Warntjes, J. B., & Lundberg, P. (2013). Application of quantitative MRI for brain tissue segmentation at 1.5 T and 3.0 T field strengths. *PloS one*, *8*(9), e74795.

Westin, C. F., Knutsson, H., Pasternak, O., Szczepankiewicz, F., Özarslan, E., Van Westen, D., Mattisson, C., Bogren, M., O'donnell, L. J., Kubicki, M., Topgaard, D. & Nilsson, M. 2016a. Q-space trajectory imaging for multidimensional diffusion MRI of the human brain. *Neuroimage,* 135, 345-62.

Zhang, H., Schneider, T., Wheeler-Kingshott, C.A., Alexander, D.C., 2012. NODDI: practical in vivo neurite orientation dispersion and density imaging of the human brain. *NeuroImage* 61, 1000–1016.

Zhou, Chenhong, et al. "Learning contextual and attentive information for brain tumor segmentation." *International MICCAI Brainlesion Workshop*. Springer, Cham, 2018.

Zou, Z., Shi, Z., Guo,Y. and Ye, J. (2019), “Object Detection in 20 Years: A Survey”, https://arxiv.org/abs/1905.05055

Özarslan E., 2009. Compartment shape anisotropy (CSA) revealed by double pulsed field gradient MR. *J. Magn. Reson.* 199(1), 56–67.

Özarslan E., Basser P.J., 2008. Microscopic anisotropy revealed by NMR double pulsed field gradient experiments with arbitrary timing parameters. *J. Chem. Phys.* 128(15), 154511.

Özarslan E., Koay C.G., Shepherd T.M., Komlosh M.E., Irfanoglu M.O., Pierpaoli C., Basser P.J., 2013. Mean apparent propagator (MAP) MRI: a novel diffusion imaging method for mapping tissue microstructure. *NeuroImage* 78, 16–32.